Zeeman Relaxation of Cold Atomic Iron and Nickel in Collisions with ^{3}He

Cort Johnson,[1,2] Bonna Newman,[1,2] Nathan Brahms,[1,2] John Doyle,[3,2] Dan Kleppner,[1,2] and Tom Greytak[1,2]

[1]*Massachusetts Institute of Technology*
[2]*Harvard / MIT Center for Ultracold Atoms*
[3]*Harvard University*

(Dated: July 12, 2009)

We have measured the ratio γ of the diffusion cross-section to the angular momentum reorientation cross-section in the colliding Fe–^{3}He and Ni–^{3}He systems. Nickel (Ni) and iron (Fe) atoms are introduced via laser ablation into an cryogenically cooled experimental cell containing cold (< 1 K) ^{3}He buffer gas. Elastic collisions rapidly cool the translational temperature of the ablated atoms to the ^{3}He temperature. γ is extracted by measuring the decays of the atomic Zeeman sublevels. We find $\gamma_{\mathrm{Ni}-^3\mathrm{He}} = 5\times10^3$ and $\gamma_{\mathrm{Fe}-^3\mathrm{He}} \leq 3\times10^3$ at 0.75 K in a 0.8 T magnetic field. These measurements provide further evidence of submerged shell supression of Zeeman relaxation as studied previously in transition metals and rare earth atoms [1–4]. However, our measurements indicate that angular momentum reorientation occurs more rapidly in iron and nickel than in other transition metals. Additional theoretical work is needed to explain this observation.

PACS numbers:

I. INTRODUCTION

Cooling and trapping atoms at cold and ultracold temperatures has led to unprecedented control of the external and internal atomic degrees of freedom and has aided in the advance of quantum information, precision measurement and atomic clocks, and has set the stage for quantum simulation of condensed matter systems. Successful evaporative cooling of trapped, dilute atomic gases requires a thorough understanding of elastic collisions that thermalize the sample and inelastic processes that cause heating and atom loss. Efficient evaporation is possible only for species with a high ratio of elastic to inelastic collisions γ. For atoms with isotropic interactions, such as the alkalis, $\gamma$is typically large. Alkalis can also be conveniently laser cooled due to their simple electronic structure. For these reasons, alkalis have been the atoms of choice for the majority of ultracold atomic physics experiments. Because of the proliferation of applications for ultracold atoms, there is a natural desire to develop techniques to expand the class of atomic species that can be cooled and trapped to those with rich electronic structures and anisotropic interaction potentials. Of particular interest are systems with large magnetic dipole-dipole interactions, such as dysprosium [5], which have been predicted to have novel quantum phases [6], have potential use in quantum computing [7], and demonstrate geometry-dependendant BEC stability [8, 9].

One technique capable of trapping exotic species is buffer gas cooling [10]. In buffer gas cooling, elastic collisions with a cold buffer gas, typically helium, are used to cool the atom or molecule of interest to low enough temperatures that the species may be magnetically trapped. Traditional evaporative cooling techniques may then be used to cool the species to the regime of ultracold temperatures. The flexibility of buffer gas cooling has been demonstrated by the successful trapping of many non-alkali atomic and molecular species [3, 11–17]. Buffer gas loading of magnetic traps requires about 50 collisions in order for the species-to-be-trapped to fully thermalize with the buffer gas atoms. It takes additional time for the atoms to diffuse toward the center of the trap and for the buffer gas to be removed. Thus buffer gas loading of magnetic traps has required that the orientation of the species' magnetic moment must be preserved for at least 10^4 collisions[18].

To first order, angular momentum reorientation in such collisions is dominated by the interaction between the orbital angular momentum $\mathbf{L}$ of the species and the angular momentum ℓ of the collision [19]. One therefore expects weak reorientation for species having $L = 0$, and relatively strong reorientation for species having $L \neq 0$. For instance, oxygen ($L = 1$) reorients its angular momentum in almost every collision with low-temperature He [19], while atoms such as potassium or copper ($L = 0$) have been shown to survive more than 10^6 collisions without angular momentum reorientation [12, 20]. Recent work [21, 22], however, has demonstrated the existence of a class of atoms, dubbed the "submerged shell" atoms, in which the $L \neq 0$ valence shell is protected from angular reorientation by outer lying filled shells of electrons. Experimental work with rare earth atoms [3] and the group 3–5 transition metals [2] has shown the ratio γ of collision rate to reorientation rate to be between 10^4 and 10^5 in these submerged shell atoms. In this work we expected to verify suppression of reorientation in transition metals with large magnetic moments, nickel (Ni) and iron (Fe)[1], in their collisions with low-temperature ^{3}He. We find that these atoms have $\gamma \lesssim 5 \times 10^3$. Their reorientation is more rapid than previously studied "submerged shell"

[1] Cobalt was not included in this study as the large hyperfine structure of the atom precluded spectroscopic identification of the atom's individual Zeeman states.

Atom	Configuration	Term	Moment (μ_B)
Fe	[Ar].$3d^6.4s^2$	$^5D_4$	6.005
Ni	[Ar].$3d^8.4s^2$	$^3F_4$	5.002

TABLE I: Electronic configurations of iron and nickel.

species, but we find that nickel ($\gamma = 5\times10^3$) still demonstrates significant reorientation suppression compared to strongly anisotropic species. NB2CJ3

We also introduce a technique to measure γ when temperature is finite and thermal effects are significant. We will demonstrate that a naive model that neglects these effects will lead to an overestimation of γ, and discuss how this affects the conclusions of previous work. CJ4

II. EXPERIMENTAL METHODS

We are interested in the ratio between the atom–He diffusion cross-section σ_d and the angular momentum reorientation cross-section σ_R. We are specifically concerned with reorientation from the most low-field seeking trap state, $m_J = J$, to any other Zeeman state, which will leave the magnetic trap on a time scale exponentially faster than the lifetime of the $m_J = J$ state. We can therefore write

$$\sigma_R \equiv \sum_{m'_J \neq J} \sigma_{J\to m'_J}, \tag{1}$$

$$\gamma \equiv \frac{\sigma_d}{\sigma_R}. \tag{2}$$

The diffusion cross-section may be measured by observing the diffusive decay of the atoms in our apparatus when no magnetic field is present. To measure σ_R, we apply an approximately uniform magnetic field to separate the various m_J sublevels of the atom, then measure the time constant for loss of the $m_J = J$ population as a function of the zero-field diffusion time. Extraction of the cross-section ratio from measurements of the atom decay time constants is discussed in §III.

A. Cryogenic Apparatus

The heart of our apparatus is shown in Fig. 1. The body of our experimental cell is machined from a G10 tube 7.6 cm in diameter and 30 cm in length. It is thermally anchored to the mixing chamber of a dilution refrigerator by four half-inch oxygen free high purity copper braids. Thermal conductivity along the length of the cell is provided by ∼ 1,000 0.25 mm diameter copper wires running vertically along the outer G10 cell wall. Each wire is electrically insulated from the rest to prevent eddy current heating as we ramp magnetic fields. Base temperature of the refrigerator is 30 mK resulting in a cell top temperature of ∼ 100 mK cell bottom temperature of ∼ 170 mK. A 6.6 cm sapphire window forms the bottom of the cell. Sapphire passes the UV frequencies needed for spectroscopy and has higher thermal conductivity than fused silica. The window is epoxied into the G10 body, forming a vacuum seal with the cell wall.

The cell body is housed in a cylindrical vacuum chamber with 1 mm radial clearance. A 4 T superconducting magnet fits tightly around the vacuum chamber. Clearances are made as tight as possible to enable maximum fields at the cell wall. The magnet coils can be connected at room temperature in either in a Helmholtz (constant field) or an anti-Helmholtz (trapping field) configuration. This work required only Helmholtz fields.

Buffer gas is introduced into the cell through a fill line. The fill line is connected to a vacuum chamber containing a charcoal sorb filled with ^{3}He. The vacuum chamber is thermally anchored to a 4K helium bath. For each buffer gas load, we heat the sorb with a resistive heater to ∼ 10 K. This drives helium off the sorb, through the fill line, and into the cell. Adjusting the duration and power of the heater pulse allows us to vary the amount of loaded buffer gas in a predictable manner.

B. Spectroscopy

Fe and Ni atoms are produced via ablation of metallic targets mounted inside the cell. Ablation is performed with a 10 ns pulse from a doubled YAG laser at 532 nm. For this work, we used pulse energies ∼ 15 mJ. We probe atomic density, lifetime, and temperature via balanced absorption spectroscopy on the $^5D_4 \to {}^5F_5$ transition at 248 nm in Fe and the $^3F_4 \to {}^3G_5$ transition at 232 nm in Ni. The light in both cases was produced from a dye laser doubled in a resonant cavity containing a BBO crystal.

Optical access into the cryogenic apparatus is limited to a single port through the bottom. Beam steering optics mounted to the bottom of the dewar direct the laser into the cell. The beam retroreflects from a mirror at the top of the cell and the exiting light is detected on a photomultipler tube (Hamamatsu H6780-04 [23]).

C. Measurement of the diffusion lifetime

The lifetime of the atoms at zero-field is set by their diffusion through the buffer gas to the cell wall. The

[2] We should probably cite Killian Sr*, Takami *Yb** work, theory on Th-Yb collisions, work with O, maybe some Weinstein work, etc.

[3] I've cited only O–He collisions, not Sr–Sr, Yb–Yb, etc. because this is an $L \neq 0$–noble gas collision paper. I can be persuaded otherwise if people disagree.

[4] Please read and comment on new section added immediately before Conclusion discussing previous work.

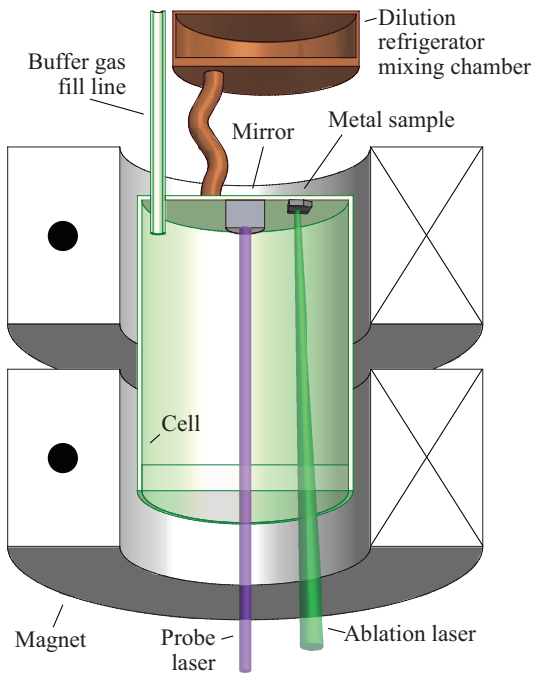

FIG. 1: (color online) Schematic of the cryogenic apparatus. The magnet can operate in Helmholtz (shown) or anti-Helmholtz configurations.

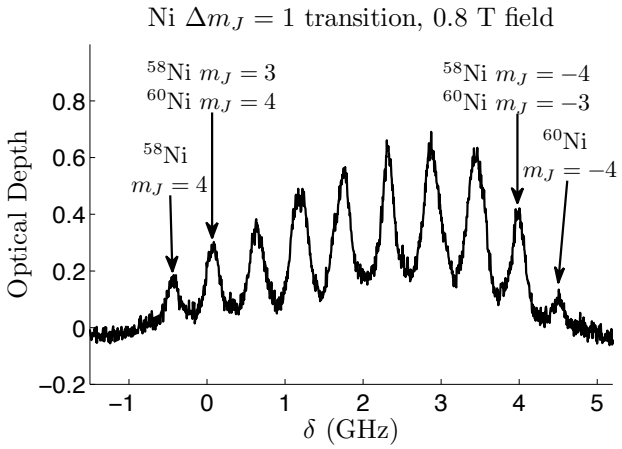

FIG. 2: Nickel optical depth vs. frequency (arbitrary zero) in homogeneous (Helmholtz) field. Each isotope has 9 lines corresponding to the 9 m_J states. The Zeeman and isotope shifts are roughly equal at 0.8 T fields, causing lines of different isotopes to overlap. Measurements of the $m_J = J$ state lifetime are performed by parking on the $m_J = 4$ transition peak and measuring the optical depth versus time.

diffusion lifetime τ_d is proportional to the buffer gas density in the cell (see equation 4). A measurement of τ_d is therefore a relative measurement of n_{BG}.

To make the lifetime measurement the frequency of the laser is tuned to the atomic resonance of interest. The laser frequency is scanned repeatedly over the absorption feature as atoms are introduced into the cell. The number of absorbing atoms in the probe beam is measured by integrating the spectrum over the atomic line. Low frequency noise can be eliminated by subtracting the signal at a dark portion of the spectrum from this integral. We fit the decay in this integrated optical depth to a single exponential decay function to determine the diffusion lifetime τ_d. Because the laser scan has a maximum bandwidth of ~ 30 Hz, decays faster than this are measured by parking the laser frequency at the absorption peak. However, this latter method is subject to low frequency noise.

D. Measurement of the $m_J = J$ lifetime

To measure the lifetime τ_J of the $m_J = J$ state, we must resolve an absorption peak from the $m_J = J$ ground state. This is accomplished by turning on a homogeneous magnetic field, thereby splitting the atom's Zeeman sublevels. The lines are also broadened, due to field inhomogeneity within the magnet.

Consider a transition from a m_J ground state with Landé factor g_J to a $m_J + \Delta m_J$ excited state with Landé factor g_J'. The field induced frequency shift $\Delta\nu_Z$ is

$$\Delta\nu_Z = \left(g_J' \Delta m_J + (g_J' - g_J) m_J\right) \frac{\mu_B B}{h} \qquad (3)$$

where h is Planck's constant. Selection rules require $\Delta m_J = 0, \pm 1$. The first term in (3) is generally much larger than the second, yielding three manifolds of equally spaced peaks, each corresponding to a ground state Zeeman sublevel.

The $m_J = J$ state is identified by tuning to the $\Delta m_J = 1$ set of peaks as shown in Fig. 2.[5] Nickel's spectrum in a magnetic field is relatively simple because the most common isotopes, ^{58}Ni,^{60}Ni, and ^{62}Ni, have no nuclear spin and hyperfine effects are absent. Each isotope splits into 9 lines, corresponding to the m_J sublevels. The Zeeman splitting at $B \sim 0.8$ T is approximately equal to the isotope shift between ^{58}Ni and ^{60}Ni. As a result, transitions from the ^{58}Ni m_J state overlap with ^{60}Ni transitions from the $m_J + 1$ state. Only the ^{58}Ni $m_J = J$ and ^{60}Ni $m_J = -J$ states do not experience any overlap. We measure τ_J by tuning the laser frequency to the fully resolved ^{58}Ni $m_J = 4$ absorption peak and observing the decay of the absorption signal. The most abundant iron isotopes (^{56}Fe and ^{54}Fe) are also $J = 4$ species without hyperfine structure, so the spectroscopic methods outlined above also apply to Fe. We choose to operate at 0.8 T with Ni and 1.0 T with Fe, as these are the highest fields at which the spectra are easily interpreted and at which the absorption lines are not too broadened to achieve good signal-to-noise.

[5] Clebsch-Gordan coefficients suppress the $m_J = J$ peak in the $\Delta m_J = -1$ and $\Delta m_J = 0$ manifolds.

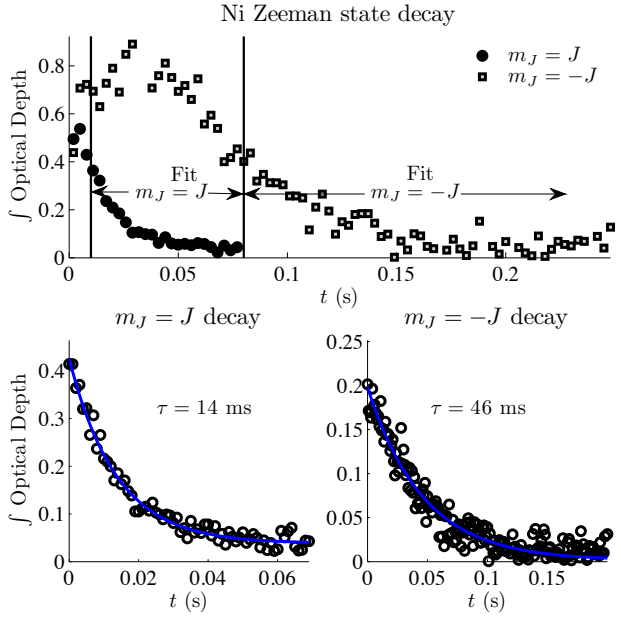

FIG. 3: (color online) Nickel $m_J = J$ and $m_J = -J$ optical depth (integrated over the atomic line) versus time with fits to lifetime. The $m_J = -J$ state experiences an initial increase in optical depth because higher Zeeman states are relaxing into the $m_J = -J$ state.

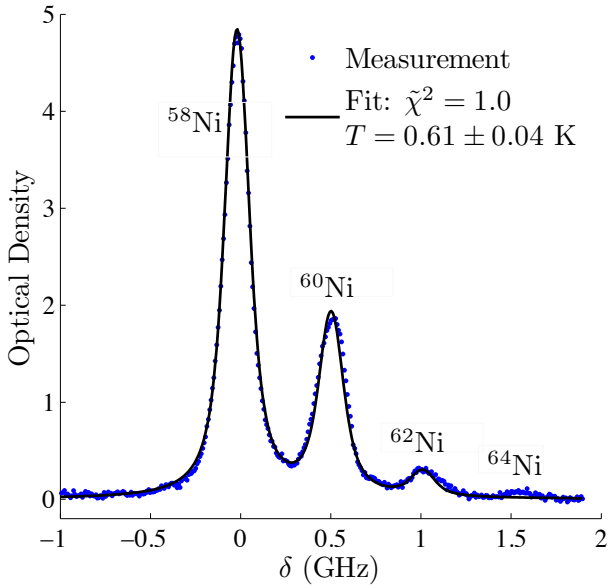

FIG. 4: (color online) Nickel zero-field optical depth versus frequency 50 ms after ablation. Frequency zero set to ^{58}Ni resonance. Temperature and density are found by fitting to a Voigt profile.

Measuring τ_J was particularly difficult for iron because the observed lifetimes were very short at all buffer gas densities. Immediately after ablation we typically see an absorption signal that decays in 2-3 milliseconds. This signal occurs at all buffer gas densities and is present when the laser is parked near, but not necessarily on, a Zeeman level resonance peak. We associate this transient signal with the decay of higher order diffusion modes. Because it is unrelated to the momentum reorientation we are trying to measure, we typically ignore data taken in the first 10 ms after ablation. For example, Ni τ_J were found using data taken between 10 ms – 50 ms after ablation. However, due to Fe's rapid Zeeman relaxation, the absorption signal was too small to be measured after 10 ms. We therefore measured τ_J for Fe starting only 5 ms after ablation.

Using the above procedure we can also study the dynamics of the $m_J = -J$ most high-field seeking state. For each buffer gas density we measure τ_{-J} and compare it with τ_d. In the limit of zero temperature, the $m_J = -J$ state does not experience loss from Zeeman relaxation, and we should find $\tau_{-J} = \tau_d$. Fig. 3 shows an example of $m_J = J$ and $m_J = -J$ state decay with fits to a single exponential lifetime.

E. Temperature Measurement

At atom temperatures greater than or comparable to the atomic Zeeman splitting, 670 mK at 0.8 T for Ni, thermal excitations cause the observed loss rate of the $m_J = J$ state to diverge from the Zeeman relaxation rate. In order to extract σ_R from the observed loss rate, we measure the temperature of our atoms from broadening of the zero-field spectrum. Fig. 4 shows the zero-field spectrum of the $a^3F_4 \rightarrow y^3G_5$ transition of Ni at 232 nm, taken 50 ms after ablation. The optical detuning is calibrated using a Fabry-Perot cavity. The observed atom density is $\sim 3 \times 10^9$ cm^{-3}, corresponding to 3×10^{11} Ni atoms in the cell. The temperature of the atoms is determined by fitting to a Voigt profile [24].

Fig. 5 shows the temperature of the Ni atoms as a function of time for three buffer gas densities. Thermal excitations have the greatest impact at high buffer gas densities, where the Zeeman relaxation rate is much faster than the diffusion rate. In our analysis, we shall use the average measured Ni temperature at high densities, 750 mK.

The zero-field spectrum could potentially be broadened due to trapped fluxes in the superconducting magnet. These have previously been measured to be ≤ 10 gauss [25], yielding a systematic uncertainty of $^{+0}_{-110}$ mK.

III. LIFETIME MODELS

A. Model in the limit of zero temperature

At high buffer gas densities and in the limit of zero temperature, atoms are lost from the $m_J = J$ state due to two primary mechanisms. First, atoms diffuse via elastic collisions until they reach the cell walls, where they stick.

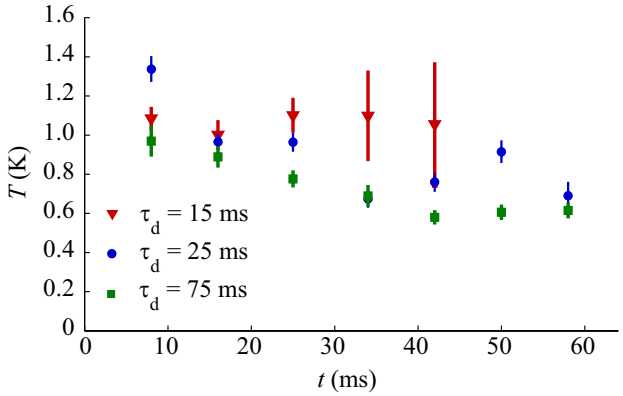

FIG. 5: Nickel temperature versus time. Temperature measurements were made at 3 different buffer gas densities. The atoms cool only slightly over the time scale of our τ_J measurements. The temperature is slightly higher at lower buffer gas densities.

Second, atoms may experience Zeeman relaxation. In this section we ignore collisions that repopulate the $m_J = J$ state once the atom has relaxed into a lower energy state. We will include this finite temperature effect in Section III B.

In a cylindrical cell of radius $R_{\rm cell}$ and length $L_{\rm cell}$, the lifetime due to diffusion, for atoms in the lowest order diffusion mode, is [26]

$$\tau_d = \frac{n_b\,\sigma_d}{\bar{v}\,G}, \tag{4}$$

$$G = \frac{3\pi}{32}\left(\frac{\pi^2}{L_{\rm cell}^2} + \frac{j_{01}^2}{R_{\rm cell}^2}\right). \tag{5}$$

where $j_{01} = 2.40483\ldots$ is the first zero of the Bessel function $J_0(z)$, n_b is the buffer gas density, and $\bar{v}$ is the mean relative velocity of the colliding atom–He system. We can ensure that all atoms are in the lowest order diffusion mode by a waiting for a few multiples of τ_d before measuring the atom lifetime.

At zero temperature, the lifetime of atoms in the $m_J = J$ state is the reciprocal sum of the diffusion lifetime and the lifetime due to Zeeman relaxation:

$$\tau_J = \left(\frac{1}{\tau_d} + \bar{v}\,\sigma_R\,n_b\right)^{-1} \tag{6}$$

Unfortunately we do not have an absolute calibration of n_b. However, we can use (4) to eliminate n_b from (6). Doing this, and replacing σ_d/σ_R with γ, we find

$$\tau_J = \frac{\tau_d}{1 + \tau_d^2\,\bar{v}^2\,G/\gamma}. \tag{7}$$

If the temperature T were much less than the Zeeman splitting $g_J\mu_B B$, we could measure γ by measuring τ_J as a function of τ_d (measured at zero magnetic field), and fitting to (7). However, as we shall show in the next section, this model breaks down when $k_BT \approx g_J\mu_B B$.

B. Model at finite temperature

The previous model assumes that once a $m_J = J$ atom experiences Zeeman relaxation it remains in a lower energy Zeeman state forever; the possibility of excitation *into* the $m_J = J$ states was ignored. When the thermal energy k_BT is much less than the magnetic interaction energy, this assumption is valid as collisions do not have sufficient energy to excite atoms into states with higher m_J. However, for our experimental conditions $k_BT << g_J\mu_B B$ does not hold, and a non-negligible percentage of collisions with the buffer gas have enough energy to excite an atom into a higher energy Zeeman state. This effect slows the observed loss from the $m_J = J$ state, yielding an overestimate of γ when the zero temperature model is used. Therefore, a correct determination of γ from measured data must take thermal excitations into account.

For the above reasons a Zeeman Cascade model which includes diffusion, the dynamics of all Zeeman states, and the possibility of thermal excitation must be developed. In our model, the density n_{m_J} of each m_J level with energy E_{m_J} at temperature T evolves according to

$$\begin{aligned}\dot{n}_{m_J} = &-\Gamma_d\,n_{m_J} - \Gamma_R \sum_{m_J'<m_J} \alpha_{m_J'm_J}\,n_{m_J} \\ &- \Gamma_R \sum_{m_J'>m_J} \alpha_{m_J'm_J}\,n_{m_J}\exp\left(-\frac{(E_{m_J'} - E_{m_J})}{k_BT}\right) \\ &+ \Gamma_R \sum_{m_J'>m_J} \alpha_{m_J'm_J}\,n_{m_J'} \\ &+ \Gamma_R \sum_{m_J'<m_J} \alpha_{m_J'm_J}\,n_{m_J'}\exp\left(-\frac{(E_{m_J} - E_{m_J'})}{k_BT}\right).\end{aligned} \tag{8}$$

where $\Gamma_d \equiv 1/\tau_d$ and $\Gamma_R \equiv 1/\tau_R \equiv \sigma_R n_b \bar{v}$ are the diffusion and relaxation rates. γ is related to these quantities by $\gamma = \tau_R\,\tau_d\,G\,\bar{v}^2$. $\alpha_{m_J'm_J}$ in each summation represents the coupling between m_J and m_J' Zeeman levels, subject to

$$\sum_{m_J'=1}^{2J} \alpha_{m_J'm_J} = 1, \tag{9}$$

and

$$\alpha_{m_J'm_J} = \alpha_{m_Jm_J'} \tag{10}$$

The first term in (8) is diffusion loss, the second is Zeeman relaxation into lower energy states, the third is thermal excitation into higher energy states, the fourth is Zeeman relaxation from higher energy states, and the fifth is thermal excitation from lower energy states.

The dominant effect of thermal excitation on $m_J = J$ atoms is an alteration of their initial decay from the simple exponential predicted by the zero temperature model.

Δm_J	$\frac{\alpha_{\Delta m_J}}{\alpha_{\pm 1}}$
± 1, 2	1.0
± 3, 4	0.2
± 5, 6	0.04
± 7, 8	0.008

TABLE II: Relative rate coefficients for Zeeman relaxation with a given Δm_J, based on [19, 28].

At early times ($t \ll 1/\Gamma_R$, when all m_J states are equally populated), thermal excitations cause the $m_J = J$ state to decay more slowly than the prediction of (7). The exact scaling will depend on T, B, and the exact form of $\alpha_{m'_J m_J}$. At later times ($t > (2J+1)/\Gamma_R$), the Zeeman states approach thermal equilibrium, and the lifetimes of all m_J levels approach τ_d.

Finding the exact values of $\alpha_{m'_J m_J}$ for each transition is a significant theoretical effort [27]. The rates for iron and nickel are unknown and must be assumed. The assumptions adopted significantly affect the predicted Zeeman state dynamics. Three "selection rule" cases for Zeeman relaxation shall be considered: all transitions between Zeeman states are equally allowed, only $\Delta m_J = \pm 1$ transitions are allowed, and an intermediate regime based on calculations for thulium and general ^3P atoms [19, 28]. The relative values of α used in this third case are shown in Table II.

IV. DETERMINATION OF γ

We use the finite temperature model to fit for γ using the following method: For each value of τ_d, we simulate the $m_J = J$ state decay using a guess value of γ, a temperature of 750 mK, a magnetic field of 0.8T, and the literature-based α values from Table II. We then extract the simulated decay rate of the $m_J = J$ state over the same time interval used to extract the measured τ_J. Finally, we perform a χ^2 fit of the simulated values of τ_J to measured values to determine γ.

A. γ for Ni–^{3}He collisions

The $m_J = J$ state lifetimes are plotted with the $m_J = -J$ state lifetimes in Fig. 6. The data display the predicted qualitative trends: a region of rising τ_J at low buffer gas densities followed by a decrease in τ_J at high buffer gas densities. The $m_J = -J$ state lifetimes are approximately τ_d as expected, whereas the $m_J = J$ state lifetimes decrease with increasing τ_d. The clear differentiation between the $m_J = J$ state and $m_J = -J$ state behaviors provides convincing evidence that we are measuring Zeeman relaxation of the $m_J = J$ state.

Fig. 6 shows the best fit of the $m_J = J$ data to the finite-temperature model,yielding $\gamma = 5 \times 10^3$. Uncer-

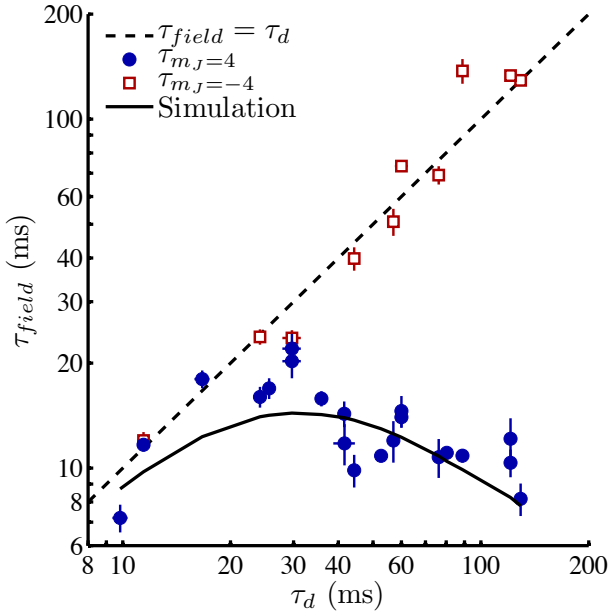

FIG. 6: (color online) Nickel $m_J = J$ and $m_J = -J$ 0.8 Tesla lifetime vs. zero-field diffusion lifetime. The dashed line has slope = 1 to demonstrate that the $m_J = -J$ atoms leave the cell by diffusion as expected. The $m_J = J$ atoms decay quickly due Zeeman relaxation in the region of high τ_d. The best fit of the $m_J = J$ data to a finite-temperature Zeeman Cascade simulation yields a value of $\gamma = 5 \times 10^3$.

tainties in the value of γ are caused by three primary effects: First, significant deviation of the data from the model leads to large statistical error bars. Second, uncertainty in the atom temperature leads to uncertainty in the thermal excitation rates used in the simulations. Third, the assumed selection rules for Δm_J affect the thermal excitation rates between Zeeman levels.

Throughout the data set there is significant deviation from the model. Most of the τ_J measurements taken at low τ_d fall above the model. The agreement is better in this diffusion dominated region for larger values of γ. However, this raises the $m_J = J$ lifetimes for all values of τ_d, resulting in poor agreement in the Zeeman relaxation dominated region. We cannot simultaneously obtain good fits in both regions, implying an unknown experimental artifact or model deficiency. At high buffer gas densities our method of measuring τ_J is no longer a reliable probe of Zeeman relaxation. After a thermal distribution of Zeeman states is established via Zeeman relaxation, atomic populations decay only by diffusion. Recall from Section II D that τ_J is fit to data taken 10–50 ms after ablation. If Zeeman relaxation occurs on time scales shorter than 10 ms this method does not accurately measure Zeeman relaxation because the $m_J = J$ state decays by a combination of Zeeman relaxation and diffusion. We attribute the scatter in the data at high buffer gas density to this effect. Finally, the scatter in the data about the model is larger uncertainty of the individual lifetime measurements. The combination of these

Selection Rule	Fit for γ
From Literature	5×10^3
All Equal	7×10^3
$\Delta m_J = 1$ only	2×10^3

TABLE III: Values of γ extracted from fits of data to Zeeman cascade simulations under various selection rules assumptions. For these fits, we used $T = 0.75$ K.

effects leads to a measured value with a 95 % confidence interval of $5^{+2.2}_{-1.6} \times 10^3$ as determined by χ^2 analysis. CJ6

The effect of temperature uncertainty on the fit for γ is quantified by systematically varying temperature in the finite temperature model. The measured temperature in Fig. 5 is 0.75 ± 0.2 K, yielding an uncertainty in γ due to temperature estimation of $\pm 1 \times 10^3$.

Finally we consider the effects of the assumed selection rules for Zeeman relaxation. For the fit in Fig. 6 we used guidance from the literature in setting realistic selection rules. However, it is impossible to quantify the accuracy of our guess. We therefore consider the effect on the fit value of γ as we vary the selection rules. One extreme case is to impose a strict selection rule that $\Delta m_J = \pm 1$. The opposite extreme is to assume that the rates into all energetically allowed states are equal. We quantify the selection rule uncertainty by fitting the entire data set to the simulation using the extremes in selection rules. The result is shown in Table III. The values of γ vary between 2×10^3 and 7×10^3. We assign a lower bound of $\gamma > 2 \times 10^3$ based on this result.

It is interesting to note that although it is the temperature of the atoms that causes the thermal excitation to occur, the larger source of uncertainty is in the selection rule assumptions. This can be understood as follows: Recall that $\Gamma_R = (\overline{v}^2 G \tau_d)/\gamma$ where $\overline{v} \propto \sqrt{T}$. As the temperature increases, the Zeeman relaxation increases proportional to temperature. However, this increase in the Zeeman relaxation rate with temperature is counteracted by the decrease in the perceived $m_J = J$ loss rate due to collisional excitations. The overall effect causes the uncertainty of the fits caused by temperature to be less important than the uncertainty caused by selection rule assumptions and systematics in the data.

B. Iron: Upper Limit on γ

Fig. 7 shows the measured τ_J vs. τ_d. The predicted region of $\tau_J \propto \tau_d$ at low buffer gas density is not observed, indicating that Zeeman relaxation occurs on a time scale faster than diffusion for the entire range of τ_d. Therefore our finite temperature model cannot be used to fit for γ. The slight rise in τ_J with increasing buffer gas is consistent with measuring a combination of Zeeman relaxation and diffusion as discussed in the previous section.

We set an upper bound of $\gamma < 3 \times 10^3$ by using conservative values for the parameters in the following expression:

$$\gamma = \tau_d \tau_R \overline{v}^2 G. \tag{11}$$

We calculate $\overline{v}$ from the temperature measured via the Voigt profile of a zero-field spectrum taken 8 ms after ablation. Recall that τ_J is a reciprocal sum of diffusion and Zeeman relaxation lifetimes. When $\tau_d = \tau_R$ the expected value of $\tau_J = \tau_d/2$. We assume this condition is met at our lowest buffer gas point since $2 \times \tau_d$ is within the error bar of τ_J. This yields the most conservative upper bound on γ because τ_R is at a maximum value consistent with our observation that $\tau_J < \tau_d$. We leave it as an open theoretical question to determine why angular momen-

[6] The preceding paragraph requires explanation and I anticipate feedback from everyone. The reduced χ^2 ($\tilde{\chi}^2$) SHOULD be approximately 1. Ours is roughly 8; obviously huge. This disturbing fact has always put a question mark about how to quote a statistical uncertainty. There are 3 ways I can think of to do χ^2 analyses which result in slightly different confidence intervals. They are based upon Chapter 11 of Bevington's "Data Reduction and Error Analysis for the Physical Sciences". I have elected to use method 3 but await your feedback.
1. Inflate the error bars until $\tilde{\chi}^2 = 1$, then find the value of γ on either side of the least squares fit value (5×10^3) for which the integrated probability of having a $\tilde{\chi}^2$ so large is less than 5 %. Much of the problem with our high $\tilde{\chi}^2$ is due to an underestimate of our measurement uncertainty. This can be seen from the large scatter in the data compared to small error bars. However, inflating the uncertainty somewhat artificially does not account for potential problems with the model. Result of this approach: $5^{+1.7}_{-1} \times 10^3$.
2. Bin the data and calculate new error bars. Unfortunately we don't have a huge amount of data for each different region of buffer gas density, so we would probably only be able to bin some of the data and use the resulting error in the binned data to infer a realistic data uncertainty for all of the data. This could be a more convincing solution, but a preliminary analysis says that this procedure still predicts a $\tilde{\chi}^2$ of at least 2. The binning of the data would result in a larger error bar because we would end up having less degrees of freedom in the analysis (see Bevington). Error bars would depend on how many bins were created, which data was binned, etc. So there's subjectivity here as well. I didn't generate any hard numbers but a rough estimate of the worst case scenario gives $5^{+2.9}_{-1.9} \times 10^3$.
3. Use an F test. This method uses the probability distribution for the RATIO of two χ^2 statistics. It is a less ambiguous test than the previous methods because χ^2 tests measure both the scatter in the data as well as the validity of the model function. Unless I'm misunderstanding the test, we can throw out the null hypothesis that two values of γ are statistically identical by comparing the ratio of their resulting χ^2. When their ratio becomes > 2.12 (for our 20 degrees of freedom) we know with 95 % confidence that the null hypothesis is false. We quote the least squares value as γ with asymmetric error bars determined by the F test. This is what I have stated above in the text. This type of application of the F test (to assign error bars to a fit parameter) is different than the applications I found in the book or on the web. In those cases they were mostly comparing different models, not different values of a fit parameter in the same model. I would appreciate people's opinion on whether or not they think my approach is valid.

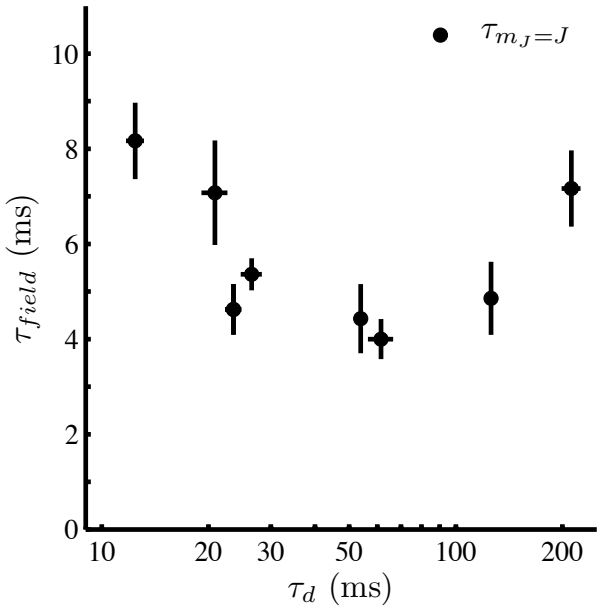

FIG. 7: Iron $m_J = J$ 1.0 Tesla lifetime vs. zero-field diffusion lifetime. There is no region of τ_d for which τ_J increases. This indicates that Zeeman relaxation is the dominant loss mechanism for the entire range of data.

tum reorientation is more rapid in iron than in any other observed transition metal.

C. Impact on previous work

We have demonstrated above that thermal effects impact the value of γ extracted from $m_J = J$ decay data when the Zeeman splitting between neighboring m_J states is comparable to thermal energy. In previous work with rare earth atoms and transition metals, finite temperature effects were ignored. It was assumed that the measured exponential decay rate of the $m_J = J$ atoms was equal to the Zeeman relaxation rate. We now examine the validity of such assumptions in the context of the present work.

Thermal effects are significant when $\frac{g_J B}{T} \sim \frac{k_B}{\mu_B} = 1.488$. For example, the nickel measurement was taken at $\frac{g_J B}{T} \sim 1.3$. The rare earth γ values were measured in an anti-Helmholtz trap with field strengths varying between 1 and 3 Tesla [3]. Thermal excitations were ignored because trap depths (ranging from 4.5K to 11K) were significantly higher than the temperature of the buffer gas (800mK). However, the range of $\frac{g_J B}{T}$ varied between 2.3 and 4.7 (assuming 3T trap) or 0.8 to 1.7 (assuming 1T trap). When a 1T trap was used, thermal effects would certainly be significant. Furthermore, the stated field occurred at the cell wall. Most trapped atoms experienced a weaker field because their thermal energy was significantly less than the trap depth. Therefore thermal effects were likely relevant for all rare earth measurements. A thorough analysis would include thermal excitations discussed in §III B and the m_J dependence of the trap potential. For titanium, γ was measured in both a 3.8T anti-Helmholtz trap and a 2.3T homogeneous field [2, 29]. Given the measured temperatures, in both cases $\frac{g_J B}{T} \sim 1.4$ and ignoring thermal effects results in an overestimate of γ. However, the effect will be less significant in Ti ($J = 2$) than Ni ($J = 4$) because the $m_J = J$ atoms decay through fewer Zeeman states.

V. CONCLUSION

A study of collisions between the most low-field seeking state of nickel and iron with ^{3}He has been performed. Although the elastic and inelastic collision rates each depend on the buffer gas density, a method has been developed to measure their ratio γ without direct knowledge of buffer gas density. For our experimental conditions the energy splitting between adjacent Zeeman levels was comparable to the thermal energy of the atomic sample. We could not operate at higher fields because magnetic broadening of the atomic resonances decreased our signal to noise to intolerable levels. Under these circumstances, thermal excitation into the $m_J = J$ state alter its perceived Zeeman relaxation rate and must be included in the analysis. The ratio of elastic to inelastic collisions γ for the Ni-He system has been found to be $5^{+2.2}_{-1.6}(stat) \pm 1(sys) \times 10^3$, assuming the Zeeman state relaxation coupling coefficients of Table II. A change in the assumed relaxation coupling coefficients alters the predicted deviation of the $m_J = J$ state decay rate from the pure Zeeman relaxation rate Γ_R. We have also set an upper limit of 3×10^3 on γ for the Fe-He system of 3×10^3.

The nickel measurement further demonstrates the phenomenon that inelastic processes are suppressed in transition metal-helium collisions. The anisotropy of the collision is small because the coulomb repulsion of the helium atom by the full outer $4s$ electronic shell in the transition metal prevents the helium electronic cloud from sampling the anisotropic d-shell valence electrons. The small interaction anisotropy results in a large value for γ. However, our measurements indicate that angular momentum reorientation occurs more rapidly in iron and nickel than in other transition metals [2]. Additional theoretical work is needed to explain this observation. Finally, low γ for iron and nickel lead to inefficient loading of $m_J = J$ atoms into a magnetic trap using the buffer gas loading technique.

[1] T. Tscherbul, P. Zhang, H. Sadeghpour, A. Dalgarno, N. Brahms, Y. Au, and J. Doyle (????).

[2] C. I. Hancox, S. C. Doret, M. T. Hummon, R. V. Krems, and J. M. Doyle, Phys. Rev. Lett. **94**, 013201 (2005).

[3] C. I. Hancox, S. C. Doret, M. T. Hummon, L. Luo, and J. M. Doyle, Nature (London) **431**, 281 (2004).

[4] A. Buchachenko, G. Chaasiski, and M. Szczniak, The European Physical Journal D **45**, 147 (2007), URL `http://dx.doi.org/10.1140/epjd/e2006-00263-3`.

[5] B. Newman, N. Brahmd, Y. S. Au, C. Johnson, J. M. Doyle, D. Kleppner, and T. J. Greytak, Phys. Rev. A (2009), fill in details later.

[6] K. Góral, L. Santos, and M. Lewenstein, Phys. Rev. Lett. **88**, 170406 (2002).

[7] A. Derevianko and C. C. Cannon, Phys. Rev. A **70**, 062319 (2004).

[8] L. Santos, G. V. Shlyapnikov, P. Zoller, and M. Lewenstein, Phys. Rev. Lett. **85**, 1791 (2000).

[9] T. Koch, T. Lahaye, J. Metz, B. Frhlich, A. Griesmaier, and T. Pfau, Nature Phys. **4**, 218 (2008).

[10] J. M. Doyle, B. Friedrich, J. Kim, and D. Patterson, Phys. Rev. A **52**, R2515 (1995).

[11] R. deCarvalho, J. M. Doyle, B. Friedrich, T. Guillet, J. Kim, D. Patterson, and J. D. Weinstein, Eur. Phys. J. D **7**, 289 (1999).

[12] N. Brahms, B. Newman, C. Johnson, T. Greytak, D. Kleppner, and J. Doyle, Physical Review Letters **101**, 103002 (2008).

[13] S. V. Nguyen, J. S. Helton, K. Maussang, W. Ketterle, and J. M. Doyle, Physical Review A (Atomic, Molecular, and Optical Physics) **71**, 025602 (pages 3) (2005), URL `http://link.aps.org/abstract/PRA/v71/e025602`.

[14] S. V. Nguyen, S. C. Doret, C. B. Connolly, R. A. Michniak, W. Ketterle, and J. M. Doyle, Physical Review A (Atomic, Molecular, and Optical Physics) **72**, 060703 (pages 4) (2005), URL `http://link.aps.org/abstract/PRA/v72/e060703`.

[15] C. I. Hancox, M. T. Hummon, S. V. Nguyen, and J. M. Doyle, Phys. Rev. A **71**, 031402 (2005).

[16] M. T. Hummon, W. C. Campbell, H.-I. Lu, E. Tsikata, Y. Wang, and J. M. Doyle, Physical Review A (Atomic, Molecular, and Optical Physics) **78**, 050702 (pages 4) (2008), URL `http://link.aps.org/abstract/PRA/v78/e050702`.

[17] W. C. Campbell, E. Tsikata, H.-I. Lu, L. D. van Buuren, and J. M. Doyle, Physical Review Letters **98**, 213001 (pages 4) (2007), URL `http://link.aps.org/abstract/PRL/v98/e213001`.

[18] J. Kim, Ph.D. thesis, Harvard University (1997).

[19] R. V. Krems and A. Dalgarno, Phys. Rev. A **68**, 013406 (2003).

[20] T. Tscherbul, P. Zhang, H. Sadeghpour, A. Dalgarno, N. Brahms, Y. Au, and J. Doyle, *Collision-induced spin depolarization of alkali metal atoms in cold ^{3}he gas*, accepted for publication in Phys. Rev. A Dec. 12, 2008.

[21] R. V. Krems and A. A. Buchachenko, J. Chem. Phys. **123**, 101101 (2005).

[22] R. V. Krems, J. Klos, M. F. Rode, M. M. Szczesniak, G. Chalasinski, and A. Dalgarno, Phys. Rev. Lett. **94**, 013202 (2005).

[23] Hamamatsu sells compact PMT modules which are convenient to mount and do not require a high voltage supply: www.hamamatsu.com.

[24] W. Demtroder, *Laser spectroscopy: basic concepts and intrumentation* (springer, 2003).

[25] J. G. E. Harris, R. A. Michniak, S. V. Nguyen, W. C. Campbell, D. Egorov, S. E. Maxwell, L. D. van Buuren, and J. M. Doyle, Review of Scientific Instruments **75**, 17 (2004), URL `http://link.aip.org/link/?RSI/75/17/1`.

[26] J. B. Hasted, *Physics of Atomic Collisions* (Butterworth, 1972).

[27] Roman Krems, private communication.

[28] A. A. Buchachenko, G. Chalasinski, M. M. Szczesniak, and R. V. Krems, Phys. Rev. A **74**, 022705 (pages 6) (2006), URL `http://link.aps.org/abstract/PRA/v74/e022705`.

[29] C. I. Hancox, Ph.D. thesis, Harvard University (2005).